



Three subtropical fronts in the North Pacific: Observational evidence for mode water-induced subsurface frontogenesis

Fumiaki Kobashi,¹ Humio Mitsudera,² and Shang-Ping Xie³

Received 17 January 2006; revised 12 May 2006; accepted 9 June 2006; published 26 September 2006.

[1] Subsurface fronts in the subtropical North Pacific were investigated by constructing a high-resolution temperature climatology. Three distinct subtropical fronts (STFs) are identified, which are the southern, northern and eastern STFs according to their relative geographical locations. The southern STF extends along 19° – 21° N west of the dateline, while the northern and eastern STFs appear along 21° – 24° N and 26° N in the western and central subtropical gyre, respectively. Our analysis showed that each of these STFs is associated with large negative meridional potential vorticity (PV) gradient in the thermocline below the front. The northern STF is located on the southern edge of the Kuroshio recirculation, where the negative PV gradient occurs within a narrow density range and is maintained by the low PV core of the subtropical mode water (STMW). On the other hand, the negative PV gradient at the eastern and southern STFs spans over a wide density range. The eastern STF forms near the center axis of the subtropical gyre, north of which the upper and lower portions of the central mode water (CMW) converge, forming a thick low PV pool that maintains the negative PV gradient on the front. Similarly, at the southern STF, the negative PV gradient is due to a low PV pool to the north, with the southernmost portion of the STMW stacked above the upper CMW advected from the central subtropical gyre. It is concluded that the mode waters are essential for the North Pacific STFs.

Citation: Kobashi, F., H. Mitsudera, and S.-P. Xie (2006), Three subtropical fronts in the North Pacific: Observational evidence for mode water-induced subsurface frontogenesis, *J. Geophys. Res.*, *111*, C09033, doi:10.1029/2006JC003479.

1. Introduction

[2] In the central to southwestern subtropical gyre of the North Pacific there is a shallow eastward current named the Subtropical Countercurrent (STCC) in opposition to the broad westward flow depicted by the classical Sverdrup theory at these latitudes. The STCC accompanies a subsurface temperature and density front called the subsurface subtropical front (STF). The STCC and the STF appear persistent throughout the year and are robust features of the subtropical gyre [Uda and Hasunuma, 1969; White *et al.*, 1978].

[3] Early studies suggested that the STCC is a wind-driven flow attributable to a small trough of wind stress curl [Yoshida and Kidokoro, 1967a, 1967b] or results from frontogenesis by the meridional Ekman convergence [Roden, 1975; Welander, 1981; Cushman-Roisin, 1981]. Takeuchi [1984] used an ocean general circulation model forced by surface wind stress and heat flux, and demonstrated that

neither of these mechanisms was essential for the formation of the STCC. The quest for understanding subsurface frontogenesis under broad gyre-scale wind-forcing continues until this day.

[4] The effect of surface heat flux combined with wind stress was examined by Cushman-Roisin [1984] using a simple analytical model. He indicated that, if the vertical density structure can be expressed as a function of surface density and latitude, a thermally-driven geostrophic flow converges and generates a midgyre front similar to the STF. He suggested the convergence of geostrophic current as a possible mechanism for the STF formation, though his model depends on rather artificial eastern boundary ventilation. A theoretical model excluding the eastern boundary ventilation was first proposed by Dewar [1992] and then expanded by Kubokawa [1995, 1997]. These authors stressed on the importance of nonlinear stationary Rossby waves. Using a two-level model for a subtropical gyre, driven by Ekman pumping and meridional differential heating, Kubokawa [1997] found that, if the northwestern corner of the subtropical gyre has a small north-south gradient of surface density and weak vertical shear, a stationary Rossby wave can occur and produce a STCC-like countercurrent. Such a countercurrent appears along the boundary between vertically homogeneous fluid to the north and strongly stratified fluid to the south.

[5] Recently Kubokawa and Inui [1999] proposed another mechanism based on an idealized ocean general circulation

¹Faculty of Marine Technology, Tokyo University of Marine Science and Technology, Tokyo, Japan.

²Institute of Low Temperature Science, Hokkaido University, Sapporo, Japan.

³International Pacific Research Center and Department of Meteorology, University of Hawaii, Honolulu, Hawaii, USA.

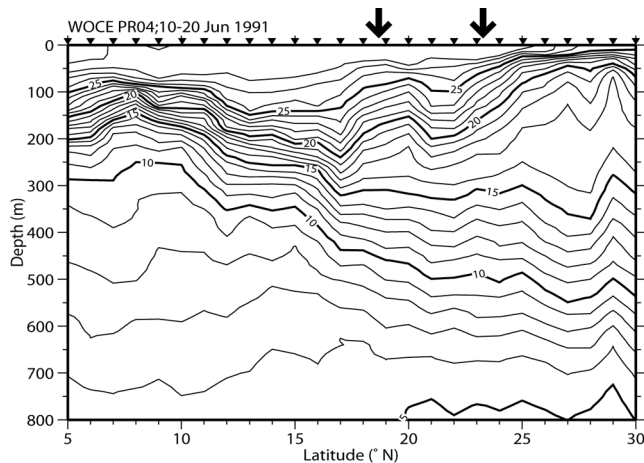


Figure 1. Temperature section along 155°E , taken by the R/V Ryofu Maru in a WOCE cruise during June 1991. Downward arrows indicate the positions of STFs. The location of observation is denoted by inverted triangles.

model simulation, in which the STCC appears along the southern edge of vertically thick layers of low potential vorticity (PV) water in the thermocline. In their model the low PV water originates in the northwestern part of subtropical gyre, subducted at the intersection of the outcrop line and a mixed layer depth front that is a narrow transition zone separating shallow and deep mixed layers. Subducted from different locations along the mixed layer depth front, the low-PV water on different isopycnals is advected southward by the subtropical gyre, eventually stacked up vertically and forming a thick low-PV pool. This thick low-PV pool requires the isopycnals in the upper thermocline to rise, leading to an eastward countercurrent on the southern edge of the low-PV pool. This mechanism was further developed by Kubokawa [1999] with a multilayer ventilated thermocline model coupled with the surface mixed layer.

[6] Many observational studies identified multiple STFs rather than a single broad front based on hydrographic data [Hasunuma and Yoshida, 1978; White and Hasunuma, 1982; White and Walker, 1985]. Similar multiple STFs have also been detected from satellite observations of sea surface temperature [Belkin *et al.*, 1998] and sea surface height data that combine satellite and acoustic Doppler current profiler measurements [Ichikawa *et al.*, 2004]. Figure 1 shows the temperature section along 155°E from the World Ocean Circulation Experiment (WOCE) Hydrographic Program (WHP), which clearly displays two thermal fronts associated with a northward shoaling of the upper main thermocline. The fronts, marked by downward arrows in Figure 1, reach a depth of about 250 m in the latitudinal bands of 17° – 20°N and 22 – 25°N , respectively. This multifrontal structure was confirmed recently by Aoki *et al.* [2002] (hereafter abbreviated as ASH) and Kobashi and Kawamura [2002]. ASH analyzed several hydrographic sections in the western and central subtropical gyre, and described the spatial structure of the two subsurface fronts: the northern front extends along 24°N from the most westernmost section along 130°E to the 179°E WHP section, while the southern front runs along 18°N parallel to the northern front up to 179°E and then suddenly jumps north to 24.5°N at the 165°W WHP

section. Constructing a long-term mean temperature climatology from historical and recent hydrographic data, Kobashi and Kawamura [2002] also found two subsurface fronts of spatial distributions similar to those of ASH, with important differences. In Kobashi and Kawamura [2002], the northern front extends typically along 24°N from 130°E to 160°W beyond the eastern edge of ASH's northern front. The southern front starts from 18°N , 130°E and continues almost zonally to a region just west of the Hawaiian Islands, with no noticeable northward shift to the east of the dateline.

[7] ASH considered these two fronts as STFs and named them the northern and southern STFs, whereas Kobashi and Kawamura [2002] regarded the northern front as an STF and the southern front as a front associated with the Hawaiian Lee Countercurrent (HLCC). The HLCC is an eastward current west of Hawaii forced by island-induced wind curls [Xie *et al.*, 2001]. General circulation models simulated an HLCC that extends from Hawaii all the way to the vicinity of the Asian coast [Xie *et al.*, 2001; Sakamoto *et al.*, 2004], similar to the southern front of Kobashi and Kawamura [2002]. Surface drifter observations, however, depicted the HLCC as rather confined in its westward extension up to the dateline [Qiu *et al.*, 1997; Yu *et al.*, 2003].

[8] Observational studies often related STFs to the distribution of mode waters. Uda and Hasunuma [1969] and Suga *et al.* [1989] pointed out that the position of STF corresponds to the southern edge of the Subtropical Mode Water (STMW), a vertically homogeneous water mass of the thermocline in the northwestern subtropical gyre [Masuzawa, 1969]. ASH confirmed the relationship between the northern STF and STMW, and found that their southern front is located along the southern edge of low PV waters that span a wide density range that includes both the STMW and the Central Mode Water (CMW [Nakamura, 1996; Suga *et al.*, 1997]). ASH suggested that the collocation of the STF and southern edge of low-PV water supports the mechanisms of Kubokawa [1997] and Kubokawa and Inui [1999], both casting mode waters in central role for STF and STCC formation.

[9] The present study examines the detailed horizontal distribution and vertical structure of the STFs and how these fronts are related to PV and mode-water distribution in the thermocline. We will construct a high-resolution temperature climatology using all available observations up to 2001. Compared with commonly used climatologies such as the World Ocean Atlas [Levitus and Boyer, 1994; Levitus *et al.*, 1994], our climatology is designed to have a high enough resolution to resolve narrow STFs. By using this high-resolution, three-dimensional climatology, our analysis extends the ASH study, which relied on several repeat hydrographic sections and snapshot WOCE transects. Long-term averaging suppresses mesoscale eddies that are dominant in the western North Pacific [Qiu, 1999; Kobashi and Kawamura, 2001], making it easier to identify the mean structure of the STFs. In addition, the use of the three-dimensional data set allows us to trace STFs continuously in space. Indeed, our analysis reveals a new third STF in the central subtropical gyre distinct from either the northern or southern fronts of ASH.

[10] The rest of the paper is organized as follows. Section 2 describes the data and procedure used to construct the climatology. Section 3 maps the spatial distribution of the

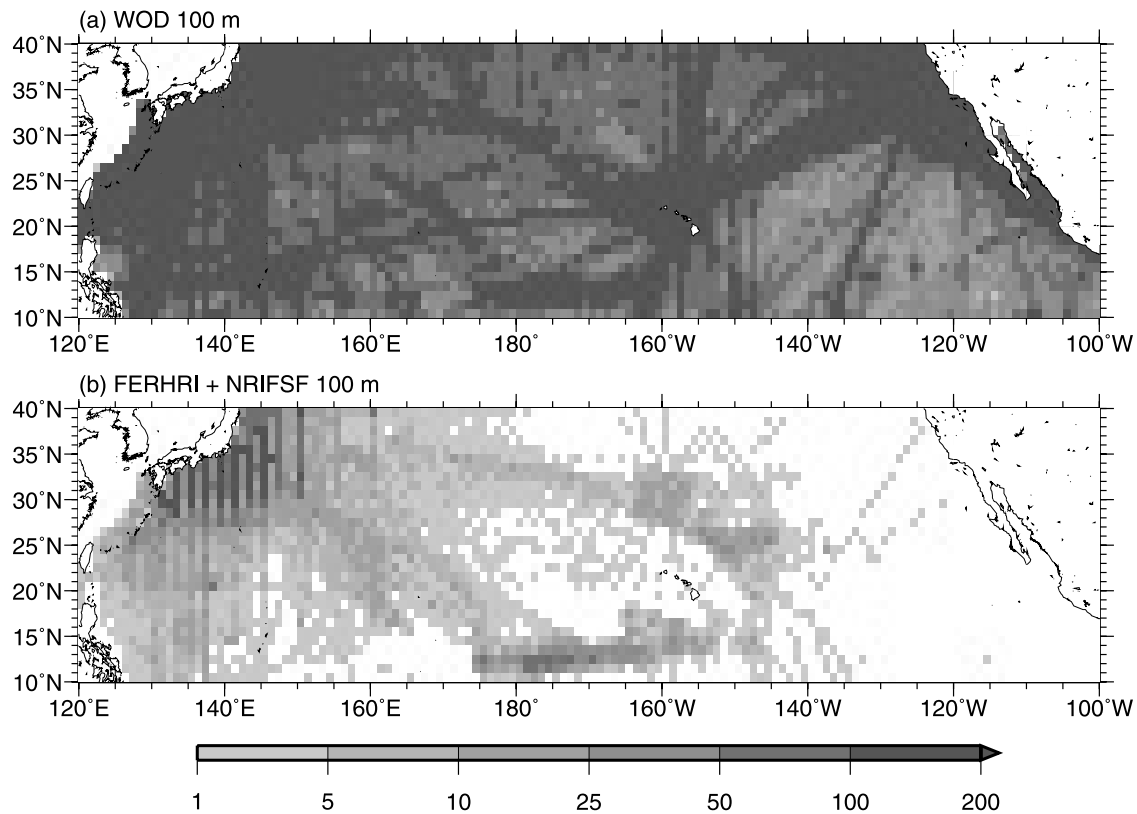


Figure 2. Distribution of temperature data used in this study, from (a) the World Ocean Database 2001 and (b) other sources from the Far Eastern Regional Hydrometeorological Research Institute (FERHRI) and the National Research Institute of Far Seas Fisheries (NRIFSF).

STFs. Section 4 investigates the thermocline structure associated with the STFs in relation to the PV distribution. We show that the PV structure is quite different among the STFs and explain the difference in terms of the distribution and circulation of mode waters. Section 5 is a summary and discusses the implications of this study.

2. Data and Processing

[11] An annual-mean temperature climatology was constructed in the North Pacific subtropical gyre. Temperature data allows us to examine the STFs, because the density structure of the upper subtropical ocean is controlled mostly by temperature. We made the climatology following *Kobashi and Kawamura* [2002], with an extensive update in data. Most of the data used in this study comes from standard depth profiles compiled in the World Ocean Database 2001 [Conkright *et al.*, 2002a]. The distribution of the data points is displayed in Figure 2a, showing a good coverage over the entire subtropical gyre with a relative paucity in regions away from coasts and major shipping lanes.

[12] The data was supplemented by two other archives. One is the data taken by Japanese fisheries training vessels during 1988–1995, obtained from the Far Seas Collection compiled by the National Research Institute of Far Seas Fisheries (NRIFSF) in Shimizu, Japan. The other comes from hydrographic surveys conducted from 1969 to 1993 by the Far Eastern Regional Hydrometeorological Research Institute (FERHRI) in Vladivostok, Russia. This was

provided by the Asia-Pacific Data Research Center (APDRC) of the International Pacific Research Center (IPRC), University of Hawaii. Inclusion of these two archives greatly increases the number of stations (Figure 2b), by 5–15% in an area north of 20°N and west of 170°E where the STFs and the STMW are distributed. Most of the additional profiles were archived at standard depths, while the rest were linearly interpolated onto the standard depths. All the data were combined into one file and then went through a quality check at each depth. Observations that differ from the average in a $5^\circ \times 5^\circ$ area by more than three standard deviations are removed.

[13] The temperature climatology was constructed on a 0.5° latitude by 2.5° longitude grid, at standard depths from the surface down to 1000 m. The grid interval is so chosen as to resolve meridionally narrow bands of the STFs while keeping enough number of observations to suppress energetic mesoscale eddies in the STF region. We first computed monthly mean each year by using a median filter with a search radius of 1° in latitude and 3.5° in longitude, and then calculated the monthly mean climatology. This procedure can reduce seasonal and year-to-year biases in the distribution of observations. The monthly mean fields were then smoothed by a Gaussian filter with an e-folding scale of 0.65° in latitude and 1.45° in longitude. This filter smoothes out features with wavelength less than approximately 350 km in the meridional direction and 700 km in the zonal direction. These filter parameters are the same as those used by *Kobashi and Kawamura* [2002]. Then, a salinity profile was assigned at

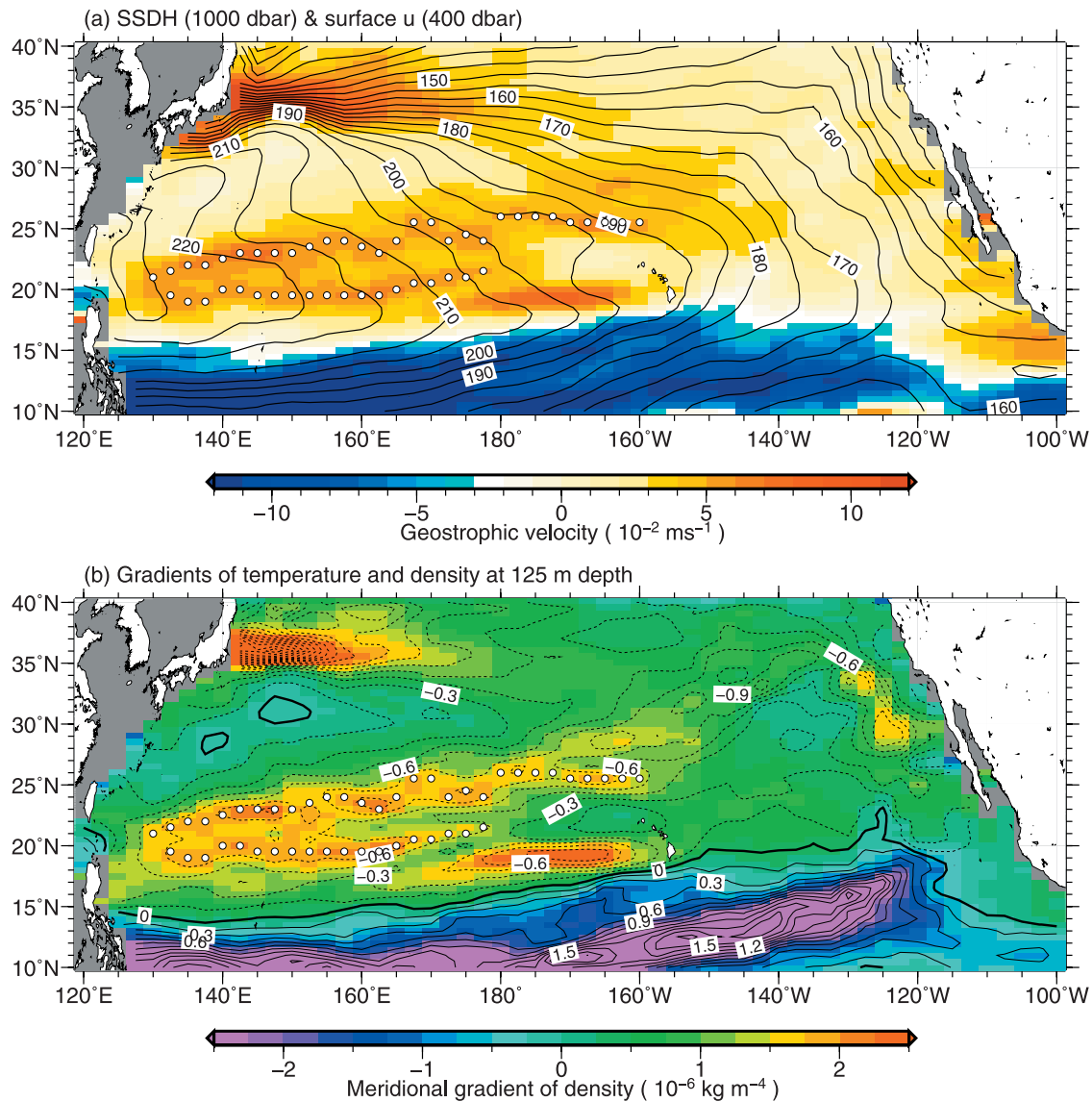


Figure 3. (a) Annual-mean surface zonal geostrophic velocity relative to 400 dbar (color shade), and sea surface dynamic height referenced to 1000 dbar (contours with an interval of 5 cm). (b) Meridional gradient of temperature (contour) and potential density (color) at 125 m depth. Open circles in both panels denote the STFs detected in this study (see text).

each grid point by using annual mean temperature and salinity relation derived from the World Ocean Atlas 2001 [Conkright *et al.*, 2002b]. Finally, the annual-mean climatology was computed by averaging the monthly climatology.

3. Three STFs

[14] This section maps the distribution of subsurface fronts by examining surface zonal geostrophic velocity relative to 400 dbar, the deepest level that STFs reach. Thus, an eastward current relative to 400 dbar roughly represents the vertically integrated strength of an STF. Figure 3a shows the surface zonal velocity together with sea surface dynamic height (SSDH) referenced to 1000 dbar. Besides the Kuroshio Extension front east of Japan, three fronts may be identified south of 30°N. The northernmost front among

them is found in the latitudinal range of 21°–26°N from 130°E to 160°W, tilting slightly to the north as it extends to the east. This is almost the same as the northern front shown by Kobashi and Kawamura [2002]. A careful look indicates that the continuity of the front is disrupted between 165°E and 180°, suggesting that it may consist of two separate fronts in the western and central North Pacific, respectively. We note that the two parts are situated in different regimes of the large-scale circulation; the western front sits on the southern edge of the anticyclonic recirculation of the Kuroshio in the midst of C-shaped SSDH contours while the eastern front extends near the central axis of the subtropical gyre where the southeast-oriented SSDH contours from the Kuroshio Extension begin turning southward. Hereafter, the fronts in the western and central North Pacific are referred to as the northern and the eastern STFs, respectively. They are

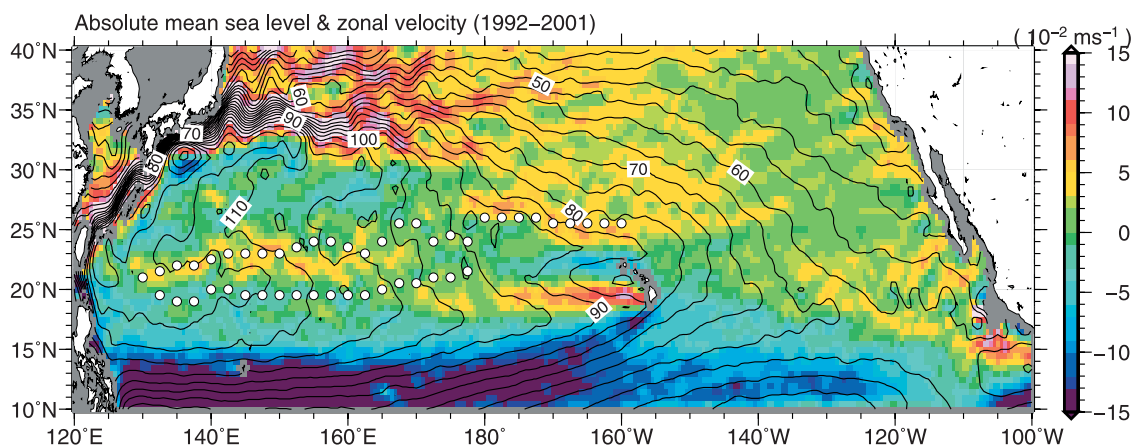


Figure 4. Absolute mean sea level during 1992–2001, computed on a 1° grid from satellite altimetry and drifter observations [from Niiler *et al.*, 2003]. Color indicates eastward geostrophic velocity and open circles denote the STFs detected in Figure 3.

typically located along 21° – 24° N and 26° N, respectively. Section 4 shows that the mode water structures to their north are very different between the northern and eastern STFs.

[15] Another front is found in the latitudinal range of 19° – 21° N from 130° E to 180° , hereafter referred to as the southern STF. This southern STF slightly veers to the north east of 160° E and is not a simple westward extension of the HLCC west of Hawaii. This appears to be consistent with the surface drifter observations of Qiu *et al.* [1997] and Yu *et al.* [2003] that the HLCC terminates near the dateline. The meridional gradient of temperature and density at 125 m depth (Figure 3b) is weaker along the STF than the HLCC front.

[16] The distribution of the STFs was further examined using an absolute mean sea level map recently produced by combining satellite altimetry and drifter data by Niiler *et al.* [2003]. Figure 4 shows the sea level and derived surface zonal geostrophic velocity. The Niiler *et al.* data set offers an independent check on the surface current field in Figure 3 derived from subsurface observations and geostrophy. In Figure 4, white dots are the same as in Figure 3, marking the STFs defined as where the zonal geostrophic velocity relative to 400 dbar reaches a meridional maximum and exceeds 5 cm s^{-1} . Overall the northern and eastern STFs agree in position between the Niiler *et al.* data set and our subsurface analysis. The discontinuity of the eastward STCC is clearer in Figure 4 than in Figure 3, taking place around 170° – 175° E. As seen in Figure 3a, the northern STF appears along the southern boundary of the Kuroshio recirculation and the eastern STF where the southeastward streamlines begin turning the corner southward.

[17] Unlike the northern and eastern fronts, the southern STF cannot be clearly recognized in Figure 4, although some discernible small patches of eastward flow along 18° N between 135° E and 165° E are suggestive of the southern STF. This does not rule out the existence of the southern STF, because the absolute sea level reflects density structure integrated over the whole water depth. As seen in Figure 1, the lower thermocline below the STFs deepens toward the north, acting to reduce the signal of the STFs on the surface velocity field through the thermal wind relation. In fact, in the

surface geostrophic velocity field calculated from the SSDH referenced to 1000 dbar, the southern STF almost vanishes while the northern and eastern STFs are still recognizable (not shown).

[18] Figure 5 assesses the seasonal persistence of STFs, showing the annual mean zonal velocity and its 95% confidence interval estimated using the monthly climatology at 5° longitude intervals between 145° E and 165° W. All the three STFs are characterized by a statistically significant peak at almost all longitudes where they are recognized as significant eastward currents. There is a quite clear separation between STF and HLCC, and between the northern and eastern STFs.

[19] Our analysis agrees with ASH on and west of their 165° E transect, with both studies identifying a pair of northern and southern STFs. ASH's southern front is located near 17° N on the 179° E section, but jumps peculiarly northward to 24.5° N at 165° W. It is now clear from our continuous mapping (Figures 3 and 4) that ASH's front at 24.5° N, 165° W is part of the eastern STF distinct from the southern front (section 4).

[20] The southern STF in Figure 3 curves slightly to the north east of 160° E. This curving is small but probably significant, consistent with the curved paths of mode waters as will be shown in section 4.4. The difference between ASH and the present study seems to come from the front that ASH found near 17° N from 179° E WHP section. Our climatology (Figure 3) suggests that on ASH's 179° E WOCE section, their front near 17° N may actually be a HLCC front. It is difficult to infer climatological fronts conclusively on the one-time WOCE section at 179° E, but there is another front near 21° N (ASH's Figure 6b), which may be part of our curved southern STF.

4. STFs and Mode Waters

[21] This section examines the structure of the STFs and infers their causes. Section 4.1 gives the physical basis for how the shallow STFs are related to the thermocline structure much deeper than the fronts themselves, and section 4.2 investigates the thermocline structure underneath the STFs.

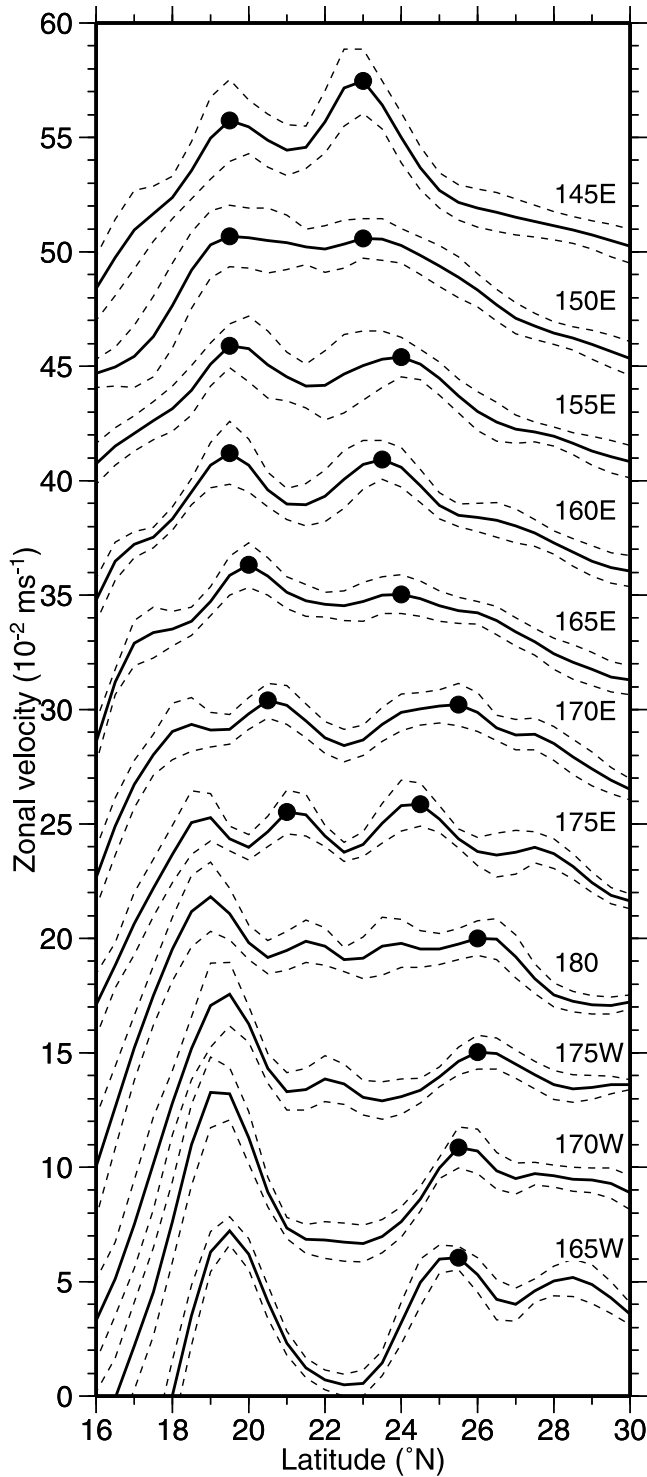


Figure 5. Meridional profiles of annual-mean surface eastward velocity (thick solid curves) and its 95% confidence interval (dashed curves), estimated from the monthly climatology, plotted every 5° longitude between 145°E and 165°W. Each profile in the panel is indicated with an offset of 5 cm s⁻¹. The STFs are denoted by solid circles.

Section 4.3 maps the distributions of major mode waters in our climatology, while section 4.4 relates them to the STFs above in the upper thermoclines.

4.1. Physical Basis for Analysis

[22] PV is an important variable for the analysis. Under the assumption of negligible relative vorticity, the PV q is expressed using a vertical coordinate of density ρ by

$$q(\rho) = -\frac{f}{\rho_0 \partial Z(\rho) / \partial \rho}, \quad (1)$$

where Z is the depth of isopycnal surface measured negative under the sea surface, f the planetary vorticity, and ρ_0 the reference density. The minus sign is introduced because $\partial Z / \partial \rho$ is negative for a stably stratified ocean. Solving for Z leads to

$$Z(\rho) = -\frac{1}{\rho_0} \int_{\rho_b}^{\rho} \left(\frac{f}{q(\rho')} \right) d\rho' + Z_0(\rho_b), \quad (2)$$

where Z_0 is the depth of the reference isopycnal surface ρ_b ($\geq \rho$). Taking the meridional derivative of this equation yields

$$\begin{aligned} \left(\frac{\partial Z(\rho)}{\partial y} \right)_{\rho} &= -\frac{1}{\rho_0} \int_{\rho_b}^{\rho} \frac{1}{q(\rho')} \left(\beta - \frac{f}{q(\rho')} \left(\frac{\partial q(\rho')}{\partial y} \right)_{\rho} \right) d\rho' + \left(\frac{\partial Z_0(\rho_b)}{\partial y} \right)_{\rho}, \end{aligned} \quad (3)$$

where the subscript ρ denotes that the partial derivative is taken a constant ρ surface. The left-hand side is a slope of isopycnal surface, and the right-hand is a vertical integration of the deviation of meridional PV gradient from the ambient gradient β . Thus, equation (3) states that the meridional slope of an isopycnal (related to zonal current) is related to the PV gradient below. Back in Cartesian coordinates, the strength of a density front

$$\left(\frac{\partial \rho}{\partial y} \right)_z = \frac{\rho_0 N^2}{g} \left(\frac{\partial Z(\rho)}{\partial y} \right)_{\rho} \quad (4)$$

differs from the isopycnal slope only by a factor proportional to the square of the Brunt-Väisälä frequency $N = \sqrt{-(g/\rho_0)(\partial \rho / \partial z)_z}$. In (4), g is the gravity acceleration.

[23] The above relation becomes clearer if we consider the PV under the quasi-geostrophic approximation,

$$q = \beta y + \frac{\partial}{\partial z} \left(\frac{f^2}{N^2} \left(\frac{\partial \psi}{\partial z} \right)_z \right), \quad (5)$$

where ψ is geostrophic stream function and relative vorticity is neglected. Taking the meridional derivative of equation (5) and using the thermal wind relation, we obtain

$$\left(\frac{\partial \rho}{\partial y} \right)_z = \frac{\rho_0 N^2}{gf} \int_{z_0}^z \left(\beta - \left(\frac{\partial q}{\partial y} \right)_z \right) dz' + \left(\frac{\partial \rho(z_0)}{\partial y} \right)_z. \quad (6)$$

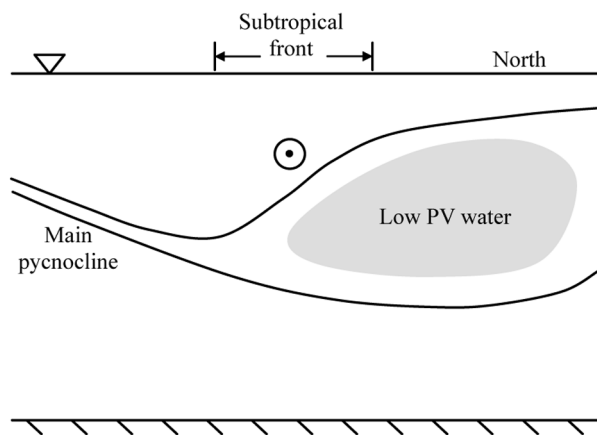


Figure 6. Schematic meridional density section across an STF.

This confirms that the frontal strength is tightly related to the PV gradient integrated over the depth below the front.

[24] Figure 6 illustrates how an STF is associated with the PV gradient. In this schematic, the main pycnocline is represented by two isopycnals. The lower isopycnal deepens northward as in a traditional subtropical gyre while the upper isopycnal shoals northward capping a wedge-like low-PV water mass. The shoaling upper pycnocline is where an STF is located. This is quite typical of STFs as in Figure 1. If we regard the lower pycnocline as deep isopycnal ρ_b in equation (3), the slope $(\partial Z_0/\partial y)_\rho$ is negative. In order for $(\partial Z/\partial y)_\rho$ to be positive (for an STF and eastward-flowing STCC), the PV gradient deviation $(\beta - (f/q)(\partial q/\partial y)_\rho)$ should take a large positive value between the upper and lower pycnoclines. In Figure 6, this is accomplished by a large negative PV gradient on the southern edge of the low-PV water mass north of the shoaling upper pycnocline.

4.2. Thermocline Structure of the STFs

[25] Here we examine the meridional and vertical structure of the STFs analyzing properties on isopycnal surfaces. The meridional density gradient $(\partial \rho/\partial y)_z$ was first calculated at the standard depths from densities between adjacent grid points, and then linearly interpolated with a density increment of $0.05 \sigma_\theta$. PV was also computed from densities between adjacent standard depths using $(f/\rho)(\Delta \sigma_\theta/\Delta z)$, where $\Delta \sigma_\theta$ is the potential density difference and Δz the depth interval, and then was interpolated to isopycnal surfaces. The PV gradient $(f/q)(\partial q/\partial y)_\rho$ was derived from the PV on isopycnal surfaces. Figure 7 shows the meridional sections of these properties at three longitudes, together with winter sea surface density calculated from the February and March climatologies.

[26] The STFs, identified as cores of strong positive density gradient $(\partial \rho/\partial y)_z$, are located just beneath the winter mixed layer and southern of near-surface high PV cells in the seasonal pycnocline. The northern and southern STFs extend down to isopycnal surfaces of $25.5\text{--}25.7 \sigma_\theta$ (Figures 7a and 7b), and the eastern STF extends slightly deeper at $26.2 \sigma_\theta$ (Figure 7c). All the STFs are anchored by negative PV gradients underneath, broadly consistent with the schematic in Figure 6 and equation (3). At shallower

depths, PV gradients are mostly greater than β , associated with reduction of the isopycnal slope of the STFs toward the surface (equation (3)), though the STFs are intensified there due to the effect of the stratification of the upper pycnocline (see equation (4)). The lower limit of the negative PV gradient layer is found around $26.7 \sigma_\theta$, which corresponds roughly to the bottom of the ventilated thermocline of the North Pacific [Talley, 1988].

[27] The vertical structure of the negative PV gradient layer underneath each STF is noticeably different from that for the others. To highlight the differences, we calculated the mean profiles of the PV gradient averaged along each STF and the 95% significant interval (Figure 8). At the northern STF, the negative PV gradient is found in a density range of $25.0\text{--}25.7 \sigma_\theta$ with a narrow peak of $25.4\text{--}25.5 \sigma_\theta$. In Figures 7a and 7b the northern front is located on the southern part of STMW that appears as a prominent low PV core centered at $25.4\text{--}25.5 \sigma_\theta$ surfaces. The negative PV gradients under the northern STF are caused by a northward decrease in PV within the STMW core.

[28] In contrast to the northern STF, the negative PV gradient at the eastern STF has a broad peak over a wide density range of $25.6\text{--}26.5 \sigma_\theta$ in the lower thermocline (Figure 8). In Figure 7c the CMW core with a vertical PV minimum is present in density of $26.1\text{--}26.5 \sigma_\theta$ north of 31°N , away from the eastern STF located around 26°N . This is quite different from the northern STF that lies adjacent to the STMW core. The negative PV gradients below the eastern front are associated with low-PV waters south of this CMW core as well as at a lighter density range of $25.7\text{--}26.1 \sigma_\theta$ that corresponds to the upper bound of the CMW.

[29] Similarly, the negative PV gradients under the southern STF have a broad peak in the density range of $24.9\text{--}26.1 \sigma_\theta$ between those for the northern and eastern STFs (Figure 8). Figures 7a and 7b indicate that these negative PV gradients are associated with low PV waters north of the front; the southernmost extension of the STMW ($24.9\text{--}25.6 \sigma_\theta$) and the upper CMW with vertically homogeneous PV in the density of $25.7\text{--}26.2 \sigma_\theta$.

[30] Thus the negative PV gradients at the STFs are closely associated with the STMW and the CMW. The situation is quite different at the HLCC front at $19^\circ\text{--}20^\circ\text{N}$ in Figure 7c. At the HLCC front, negative PV gradients occur in a deep layer from $26.2 \sigma_\theta$ to $24.0 \sigma_\theta$ near the surface. Neither of the STMW and CMW appears north of the front and makes no contributions to the negative PV gradient. The HLCC is driven by a local wind-forcing near Hawaii [Xie *et al.*, 2001], and the negative PV gradient probably results from the adjustment to this wind-forcing.

4.3. Distributions of STMW and CMW

[31] To further study the horizontal circulation of the mode waters, the PV distribution of the mode waters was mapped on isopycnals at $0.1 \sigma_\theta$ intervals between 24.8 and $26.6 \sigma_\theta$, a density range where significant negative PV gradients are observed at the STFs. Figure 9 shows the resultant PV maps every $0.2 \sigma_\theta$ with acceleration potential relative to 1000 dbar superimposed. Because of vertically uniform properties mode waters can be identified as a water of a lateral PV minimum on the isopycnal PV maps. Both STMW and CMW form in the western North Pacific east of Japan where the winter mixed layer is deep because of intense surface cooling

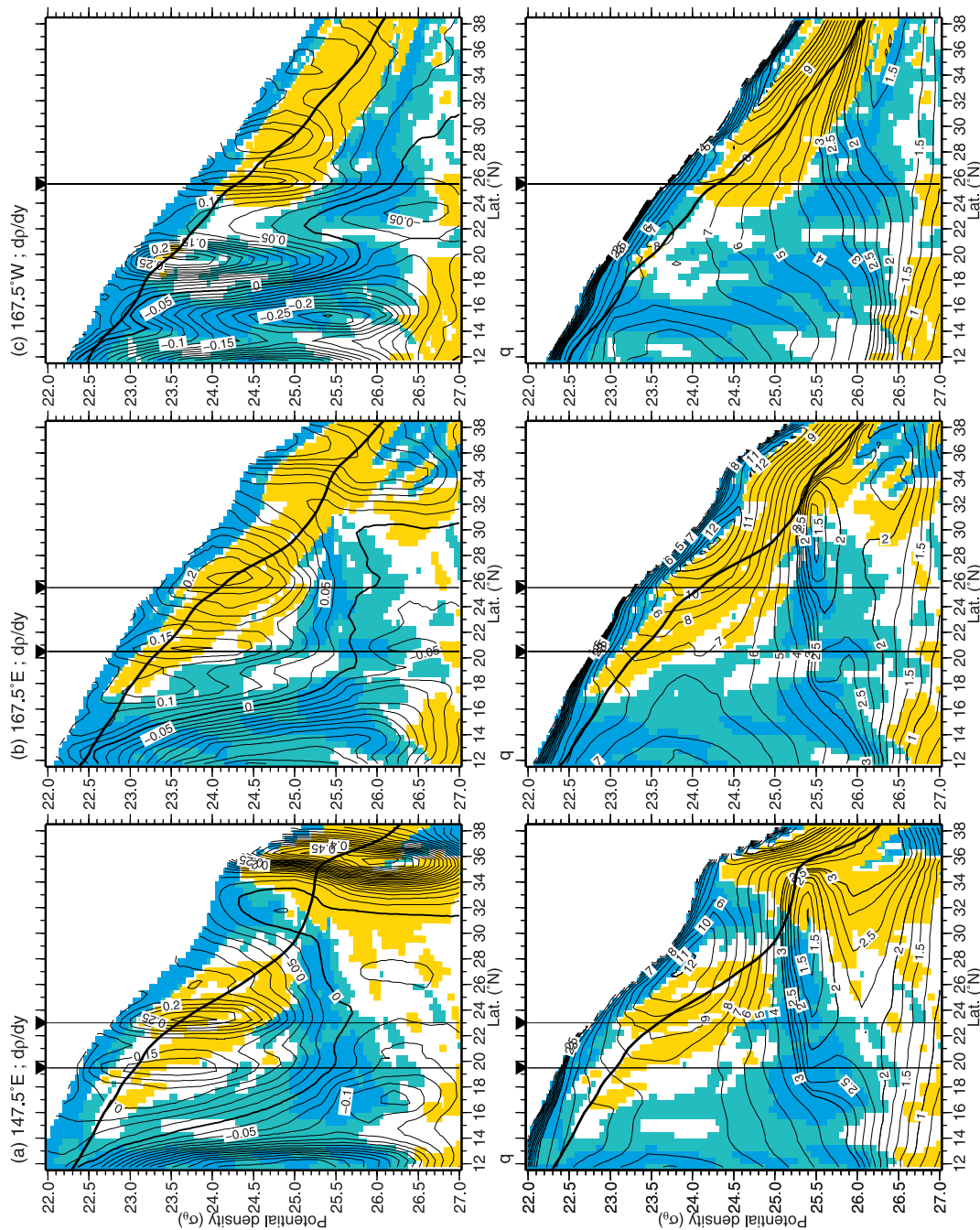


Figure 7. Meridional sections of northward density gradient (top) and PV (bottom) along (a) 147.5°E, (b) 167.5°E and (c) 167.5°W, contoured every $0.025 \times 10^{-5} \text{ kg m}^{-4}$, and every $1.0 \times 10^{-10} \text{ m}^{-1} \text{ s}^{-1}$, respectively. The contour intervals are reduced every $0.25 \times 10^{-10} \text{ m}^{-1} \text{ s}^{-1}$ for PV less than $3.0 \times 10^{-10} \text{ m}^{-1} \text{ s}^{-1}$. PV gradient $(f\bar{q})(\partial q/\partial y)_{\rho=\text{const.}}$ is shown in both panels: areas with the PV gradient greater than β are shaded with orange color, areas with less than 0 and less than $-2 \times 10^{-11} \text{ m}^{-1} \text{ s}^{-1}$ are shaded with light and dark blue color, respectively. The thick curve in each panel indicates winter mean sea surface density. The vertical lines with inverted triangles are where STFs are located; the northern and southern STFs appear in Figures 7a and 7b, and the eastern STF appears in Figure 7c.

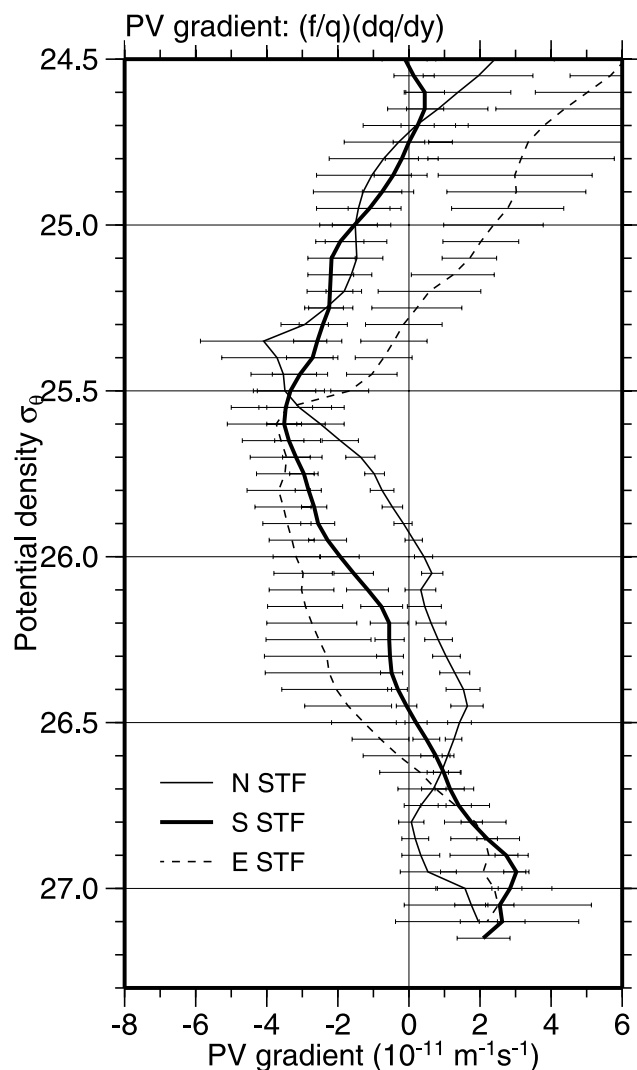


Figure 8. Mean profiles of PV gradient averaged along the northern STF between 135°E and 160°E, the southern STF between 135°E and 175°E, the eastern STF between 175°W and 160°W. The error bars indicate the 95% confidence intervals.

acting on the warm advection by the Kuroshio Extension. Theoretical [Kubokawa, 1999] and modeling [Xie *et al.*, 2000] studies have shown that an isopycnal PV minimum forms where the outcrop line intersects a mixed layer depth front that separates the deep mixed layer in the Kuroshio Extension from the shallow one in the rest of the subtropical gyre.

[32] The STMW is distributed in the northwestern subtropical gyre at the isopycnals of 24.8–25.7 σ_θ , with the lowest PV appearing on 25.4–25.5 σ_θ surfaces. As density increases, the STMW core identified as a low-PV tongue shifts to the east. The acceleration potential fields show that the low-PV tongues nearly follow the streamlines of the Kuroshio recirculation, indicating that the advection plays a primary role in the STMW distribution. These features are consistent with previous STMW studies [Suga and Hanawa, 1995; Suga *et al.*, 2004].

[33] The CMW is identified by its lateral PV minimum at isopycnals of 25.8–26.5 σ_θ . Its main body is found on 26.2–26.5 σ_θ surfaces in the central region of the northern subtropical gyre. A notable feature is a low PV tongue extending from the PV minimum in the central region to the tropical western boundary. As in Suga *et al.* [2004], the low PV tongue follows the streamlines, indicating a downstream advective spreading of the CMW.

[34] The density distribution of low-PV water was investigated to identify mode water cores. In this study, a low-PV core was defined as a vertical PV minimum with PV less than $3.0 \times 10^{-10} \text{ m}^{-1} \text{ s}^{-1}$. We have counted the number of grid points occupied by such low-PV cores between winter sea surface and the bottom of the CMW (26.5 σ_θ). The histogram of low-PV core occurrence against density displays three noticeable peaks (Figure 10). The peak at densities lighter than 25.2 σ_θ corresponds to the Eastern Subtropical Mode Water [Hautala and Roemmich, 1998; Hosoda *et al.*, 2001], which is associated with a lateral PV minimum in the eastern subtropical gyre (Figure 9). The other two peaks are the target of the present study; the sharp peak at 25.4–25.5 σ_θ and the broad peak at 26.15–26.45 σ_θ are associated with the STMW and the CMW, respectively. Although the low-PV core exists continuously between the STMW and CMW peaks, its occurrence reaches a minimum around 25.8 σ_θ , suggesting the separation of two mode waters there. The separation may also be seen on the PV maps in Figure 9, where lateral PV minima of the STMW and the CMW weaken and become obscured at 25.7–25.8 σ_θ .

[35] Figure 11 shows the distribution of the STMW and CMW cores defined as vertical minima in the density ranges of 25.2–25.7 σ_θ and 25.8–26.5 σ_θ , respectively. In the CMW layer there are often two vertical minima in PV. For such double minima, the core of lowest PV was chosen in Figure 11. Consistent with Suga *et al.* [1997], the STMW and CMW have different geographical distributions and are separated by the Kuroshio Extension front as depicted by the 12°C isotherm at 300 m depth.

[36] Although the CMW core is mostly found at density greater than 26.15 σ_θ , a lighter core of 25.8–26.1 σ_θ exists at a significant number of grid points (Figure 10). We refer to these cores as the lower and upper CMWs. In Figure 11b the grid points with an upper CMW core are marked by open triangles while those with both an upper and lower core by solid triangles. Interestingly, the upper core is situated south of the lower core in an area west of 170°W. This seems consistent with Oka and Suga [2006], who found lighter (25.8–26.2 σ_θ) and denser (26.3–26.4 σ_θ) types of the CMW located west of the dateline south and north of the Kuroshio bifurcation front (near 37–38°N at 165°E), respectively.

4.4. Mode Water-Induced PV Gradients at the STFs

[37] As mode waters form and circulate in the subtropical gyre, they produce negative PV gradients that support density front above. This subsection relates the circulation of mode waters to the formation of shallow density fronts.

4.4.1. Northern and Southern STFs

[38] It is obvious from Figure 11 that the northern STF is located along the PV front of the STMW core with large negative PV gradients, consistent with the vertical PV sections in Figure 7. At the northern STF the negative PV gradient peaks at 25.4–25.5 σ_θ in the STMW core

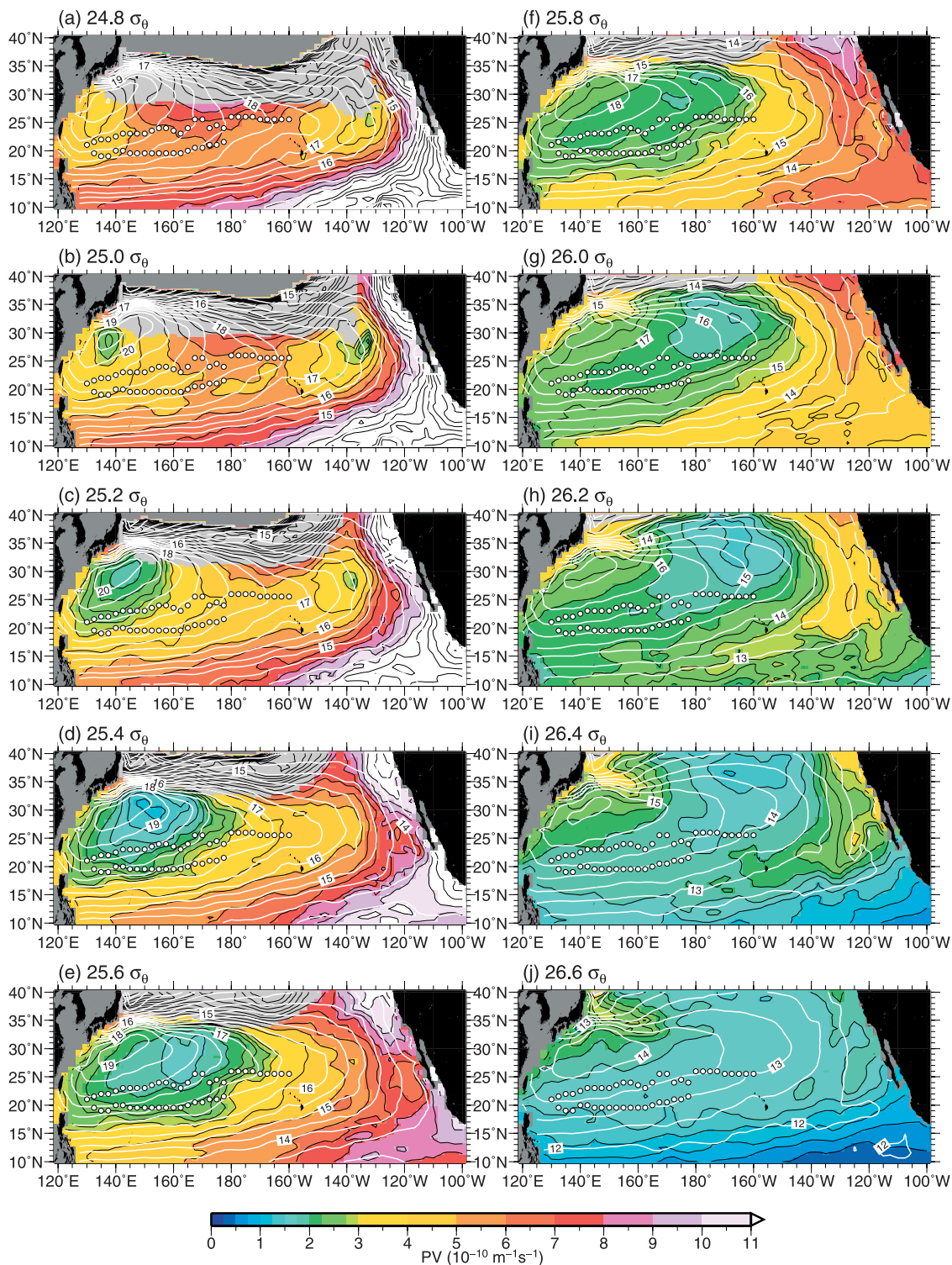


Figure 9. Map of PV on the isopycnal surfaces (a) $24.8 \sigma_\theta$, (b) $25.0 \sigma_\theta$, (c) $25.2 \sigma_\theta$, (d) $25.4 \sigma_\theta$, (e) $25.6 \sigma_\theta$, (f) $25.8 \sigma_\theta$, (g) $26.0 \sigma_\theta$, (h) $26.2 \sigma_\theta$, (i) $26.4 \sigma_\theta$ and (j) $26.6 \sigma_\theta$. Acceleration potential relative to 1000 dbar is shown by white contours with an interval of $0.5 \text{ m}^2 \text{ s}^{-2}$. Light shade indicates the area with the winter sea surface density heavier than each isopycnal, and open circles denote the STFs.

(Figure 10). The eastern limit of the northern STF near $170^\circ\text{--}175^\circ\text{E}$ is also in good agreement with that of the PV-gradient zone. These features confirm the PV front within the STMW core is the primary cause of negative PV gradients at the northern STF.

[39] The southern STF, on the other hand, is located along the southern edge of the STMW core (Figure 11). On denser isopycnal surfaces of $25.8\text{--}26.1 \sigma_\theta$, the southern STF also sits on the southern flank of a low PV tongue extending southwestward from the CMW core (Figures 9f and 9g).

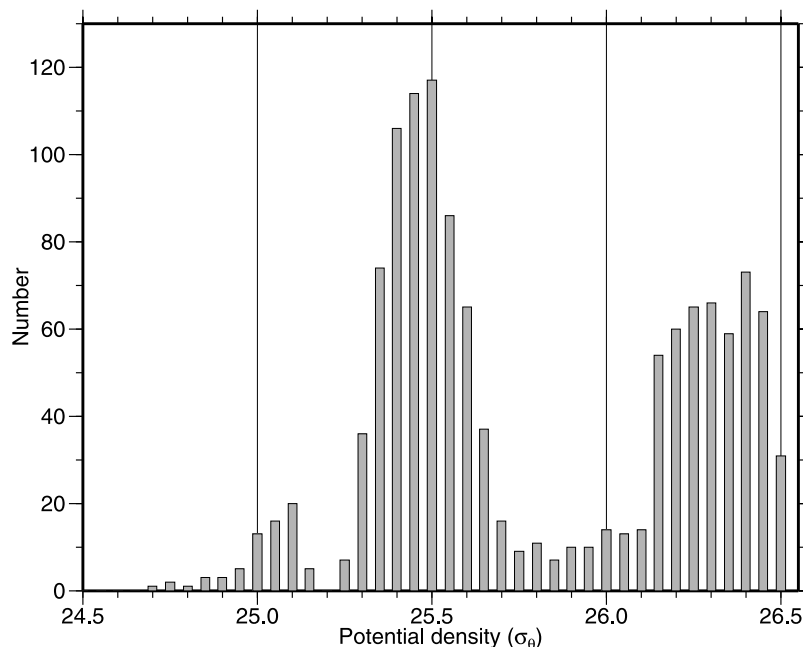


Figure 10. A histogram of the number of grid points with vertical PV minima against density.

The low PV tongue is more evident in the upper CMW than in the lower CMW. Vertical sections in Figures 7a and 7b show both the CMW and STMW contribute to the formation of the southern STF. With the southern extension of the STMW stacking above the upper CMW, large negative PV gradients form to the south, supporting the southern STF.

4.4.2. Eastern STF

[40] The eastern STF differs from the northern and southern STFs in lacking a mode water core (defined in section 4.3 as a vertical PV minimum) immediately to the north (Figure 11). Along the eastern STF, PV decreases monotonically with depth and our method of using vertical PV minimum fails to identify the CMW as a mode water core in Figure 11. Nevertheless, the CMW to the north maintains negative PV gradients at the eastern front (Figures 7 and 9).

[41] To investigate what maintains negative PV gradients over the entire density range of the CMW, we compare the CMW's circulation on isopycnals of $25.8 \sigma_\theta$ and $26.4 \sigma_\theta$, densities that represent the upper and lower CMWs, respectively (Figure 12). Let us focus on the streamlines of $16.5 \text{ m}^2 \text{ s}^{-2}$ on $25.8 \sigma_\theta$ and $14.0 \text{ m}^2 \text{ s}^{-2}$ on $26.4 \sigma_\theta$, which advect the upper and lower CMWs, respectively (Figures 9f and 9i). The CMW, forming on the northern edge of the subtropical gyre, approaches the eastern STF from the northwest on the lighter isopycnal but from the northeast on the denser one. Thus the upper and lower CMWs begin to converge toward each other immediately north of the front. *Oka and Suga* [2006] noted this convergence and suggested that the resultant vertical stacking of low PV waters would lead to the formation of an STF by the *Kubokawa and Inui* [1999] mechanism.

[42] The vertical structure of geostrophic flow direction north of each STF is shown in Figure 13. The flow direction rotates clockwise with depth from 25.0 to $26.5 \sigma_\theta$, allowing water masses from different locations to overlap in the vertical along the eastern STF. In the CMW layer, the flow veers by approximately 45° from the south in the lighter layer

to the southwest in the denser layer. Similar clockwise rotation can be seen north of the northern and southern STFs, but its magnitude is much smaller.

[43] The turning angle in geostrophic flow between density ρ_1 and ρ_2 is calculated using the expression,

$$\tan^{-1} \left(\frac{(\mathbf{u}_2 \times \mathbf{u}_1) \cdot \mathbf{k}}{(\mathbf{u}_2 \cdot \mathbf{u}_1)} \right) / \Delta\rho, \quad (7)$$

where \mathbf{u} is the geostrophic current vector with the subscript denoting the isopycnal surface, \mathbf{k} is a unit vector in the vertical direction and $\Delta\rho = \rho_2 - \rho_1$. The calculation was carried out in the density range of 25.2 – $26.4 \sigma_\theta$ that includes the STMW and CMW layers. The result is shown in Figure 14. Statistical significance was estimated based on degrees of freedom derived from the number of standard depth data within the density range. Areas above the 95% significant level are shaded. While the clockwise rotation is evident in most of the subtropical gyre, the largest spiral occurs in a relatively limited area around 25° – 31°N between 170°E and 145°W . The eastern STF is located on the southern edge of this large spiral area where the upper and lower CMWs converge and stack up in the vertical. The formation of a large low-PV pool maintains negative PV gradients at the eastern STF to the south.

[44] What causes the flow's rotation in the vertical? It is probably due to the β -spiral caused by the conservation of potential vorticity of the gyre circulation [*Stommel and Schott*, 1977]. It is related to the poleward shift of the subtropical gyre with depth [*Qu*, 2002]. The center axis of the subtropical gyre, defined as the meridional maximum of acceleration potential, was calculated on the isopycnals of the upper and lower CMWs and superimposed in Figure 12. In the western region the two axes are nearly coincident, but east of the dateline the center axis shifts to the north from 27.5°N on the lighter isopycnal to 30°N on the denser one. On a given isopycnal, flow direction changes from southeastward north

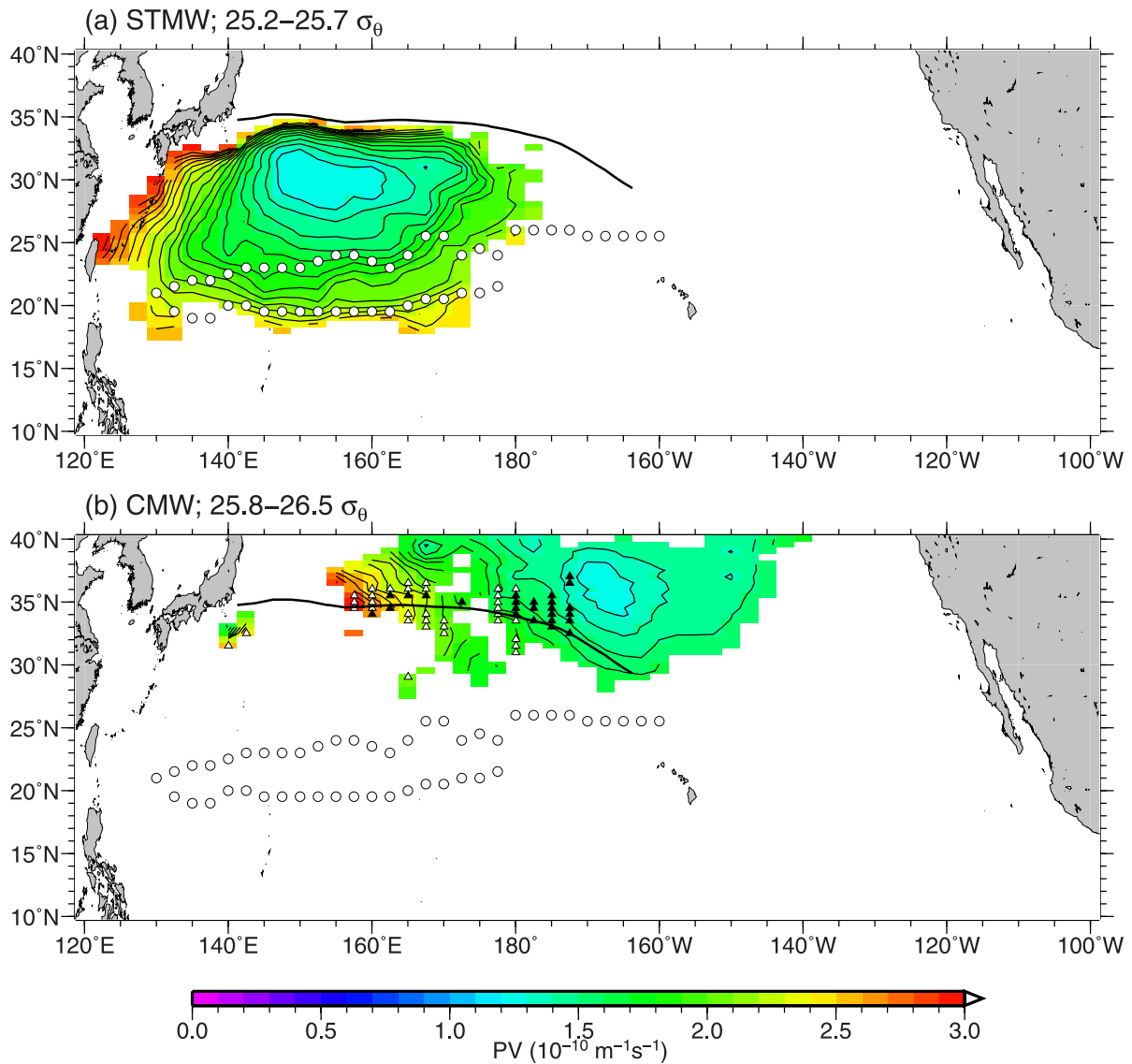


Figure 11. PV distribution of the vertical PV minima in the density range (a) 25.2–25.7 σ_θ for STMW layer and (b) 25.8–26.5 σ_θ for CMW layer. In Figure 11b, open triangles indicate the grid points where the PV minimum appears in the upper CMW layer (25.8–26.1 σ_θ), and solid triangles where it appears both in the upper and lower CMW layers. Open circles in both panels denote the STFs. A thick curve depicts the position of the Kuroshio Extension front represented by the 12°C isotherm at 300 m depth.

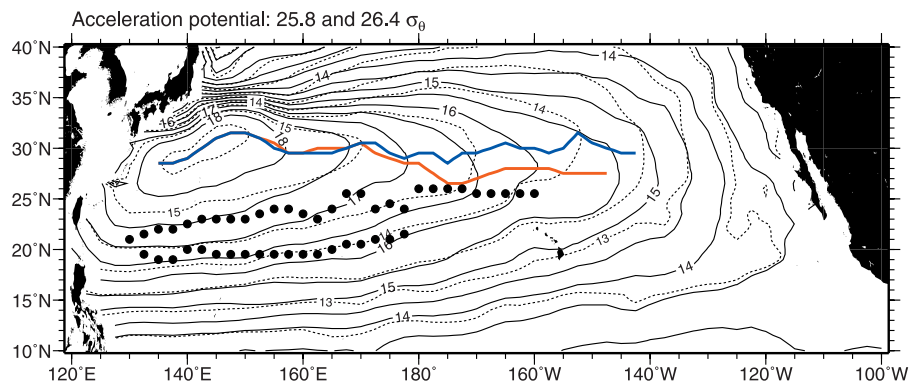


Figure 12. Acceleration potential on isopycnal surfaces of 25.8 σ_θ (solid contours) and 26.4 σ_θ (dashed contours) with an interval of 0.5 $\text{m}^2 \text{s}^{-2}$. Thick red and blue curves indicate the center axis of the subtropical gyre with the meridional maximum of the acceleration potential.

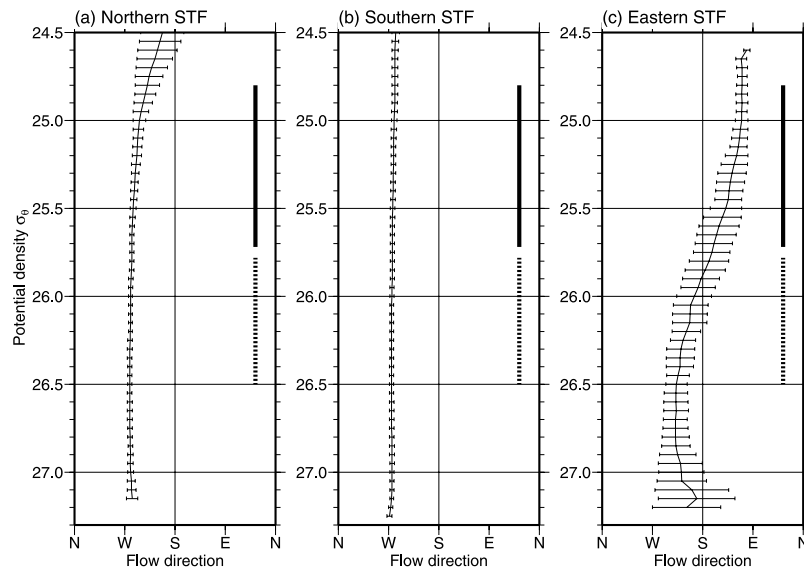


Figure 13. Vertical profiles of geostrophic flow direction as a function of density, averaged north of each front: 24° – 26° N, 140° – 160° E for the northern STF, 20° – 22° N, 140° – 160° E for the southern STF, and 27° – 29° N, 175° – 160° W for the eastern STF. The error bars indicate the standard deviation. Vertical thick and dotted lines in each panel denote the density range of STMW and CMW, respectively.

of the gyre axis to southwestward to the south. As a result, the shift of the gyre axis gives rise to the large spiral in flow direction in the vertical.

[45] Above the upper CMW on lighter isopycnal surfaces of 25.5 – $25.8 \sigma_{\theta}$, there are significant negative PV gradients along the eastern STF (Figure 8) in association with the westward intrusion of high PV just to the south (Figures 9e and 9f). This high-PV intrusion roughly coincides with the westward current west of Kauai Island that is paired with the HLCC (Figure 4), both resulting from wind curls induced by the Hawaiian Islands [Xie *et al.*, 2001] and affected by effects of the Hawaiian Islands on the ventilated thermocline [Qiu and Durland, 2002]. The high PV could be brought about by

advection of higher PV from the east by the westward current or due to Ekman upwelling induced by the islands in the northern area west of the Hawaiian Islands.

5. Discussion and Conclusions

[46] The present study investigates the spatial distributions of STFs and how these shallow subsurface fronts are related to the underlying thermocline structure by using a high-resolution temperature climatology constructed from the World Ocean Database 2001 and other sources. Our analysis revealed three distinct STFs. The southern STF is located along 19° – 21° N west of the dateline and different

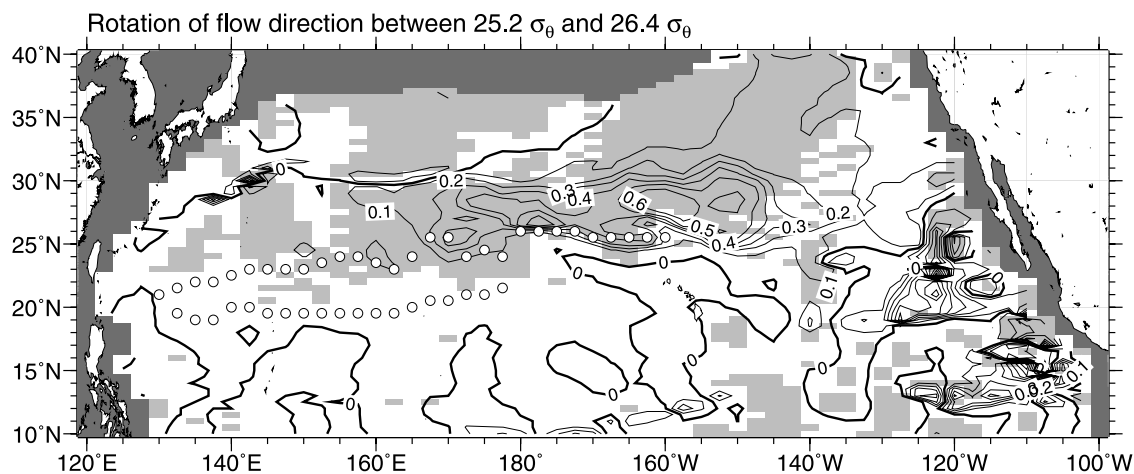


Figure 14. Distribution of changes in geostrophic flow direction between $25.2 \sigma_{\theta}$ and $26.4 \sigma_{\theta}$. A contour interval is $0.1 \text{ radian } (\text{kg m}^{-3})^{-1}$, and areas with significance at the 95% confidence limit are shaded. Positive means a clockwise rotation with density. Open circles denote the STFs.

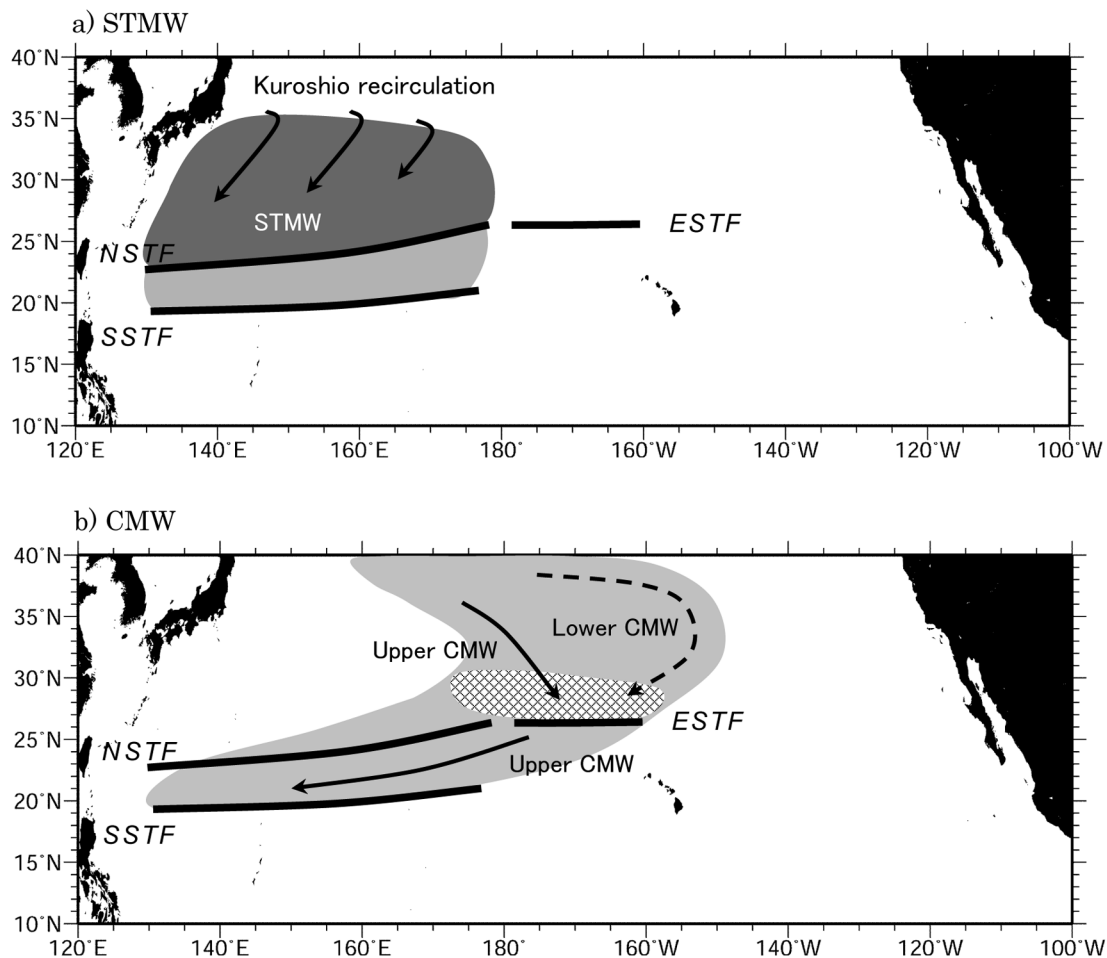


Figure 15. A schematic summary of the relationship between STF and (a) STMW and (b) CMW. The mode waters are represented by shading, while the northern, southern and eastern STF by thick lines with labels “NSTF”, “SSTF” and “ESTF”, respectively. Arrows in the upper panel indicate the advection of the STMW by the Kuroshio recirculation, while solid and dashed arrows in the lower panel represent the advection of the upper and lower CMWs by the geostrophic gyre flow. The area where the upper and lower CMWs converge is hatched in the lower panel. See text for explanation.

from a simple westward extension of the HLCC front. The northern and eastern STF are located along 21°–24°N and 26°N in the western and central subtropical gyre, respectively. These two fronts appear separated around 170°–175°E and are associated with different PV structures underneath. They can be distinguished in their positions in the large-scale circulation; the northern STF is located on the southern edge of the Kuroshio recirculation, while the eastern STF near the center axis of the broad subtropical gyre. The separation of the northern and eastern STF was confirmed in the absolute mean sea level map recently produced from satellite altimetry and drifter observations.

[47] We derived a diagnostic relation between the density front and PV gradient in the thermocline underneath. Consistent with it, all three STF are associated with large negative PV gradients in the thermocline below the fronts, and the PV gradients are tightly connected to the distribution and circulation of mode waters. The low PV structure leading to the density front formation above is quite different among the three STF, suggesting that they are formed by different

processes. Figure 15 is a schematic summary of the relationship between the STF and mode waters.

[48] For the northern STF, the negative PV gradient in the thermocline is provided by the STMW core to the north advected by the Kuroshio recirculation gyre. As suggested by ASH, the STMW corresponds to the vertically homogeneous water mass in the theoretical model of Kubokawa [1997], and the northern STF may be generated by a stationary Rossby wave. The STMW forms progressively eastward on denser isopycnals. In the Kuroshio recirculation, lighter STMW stacks above denser STMW, and negative PV gradients are found in a density range of 25.0–25.7 σ_θ at the northern STF (Figure 8). This vertical stacking of the STMW is consistent with the frontogenesis of Kubokawa and Inui [1999].

[49] Negative PV gradients at the eastern STF are observed over a wide density range of 25.6–26.5 σ_θ , a layer where the CMW is found. Both the upper (25.8–26.1 σ_θ) and lower (>26.15 σ_θ) CMWs originate from the bifurcation front of the Kuroshio Extension but are advected to the north of the eastern STF via different routes, respectively from the

northwest and northeast. As a result, the eastern STF forms along the gyre axis on the density surfaces of the upper CMW, where the vertical spiral of gyre circulation is large. The formation of a low-PV pool north of the eastern STF is consistent with the *Kubokawa and Inui* [1999] theory. Above the upper CMW ($<25.8 \sigma_\theta$), negative PV gradients persist possibly due to the influence of the Hawaii Islands on wind curls [*Xie et al.*, 2001] and/or the ventilated thermocline [*Qiu and Durland*, 2002].

[50] The negative PV gradient at the southern STF also occurs over a wide density due to the vertical stacking of the southernmost extension of the STMW above the upper CMW to the north. While the upper CMW is spread to the north of the STF by geostrophic advection, the southward spread of low PV in the STMW layer is due more than just to mean flow advection. In Figure 9, there are indications that low PV on STMW density surfaces south of the northern STF is diffused from low-PV core from the north across the streamlines, possibly by mesoscale eddies along the northern front that is dynamically unstable [*Qiu*, 1999; *Kobashi and Kawamura*, 2002]. The similar diffusive feature is visible also on maps of PV and stream function relative to 2000 dbar produced by *Suga et al.* [2004] using an isopycnally averaged climatology (their Figure 5). Unlike the eastern STF, the flow direction north of the southern STF does not show significant changes in the vertical (Figure 14). Thus the vertical stacking of mode waters is caused by not just geostrophic advection of the upper CMW but eddy diffusion of low PV from the STMW core north of the northern STF.

[51] The close connection between the STFs and the mode waters has important implications for STF variations. The northern STF has a clear seasonal cycle, strong from spring to summer and weak in fall [*Kobashi and Kawamura*, 2002]. From biannual repeat section data along 137°E, *Suga et al.* [1989] observed changes in STMW properties between winter and summer, and speculated that the arrival in the southern recirculation of a newly formed thick STMW leads to a stronger STF in spring and summer. The same relation may be expected also on interannual timescales, given that year-to-year variations have been observed in the STMW [e.g., *Suga and Hanawa*, 1995] and in the STF [*White et al.*, 1978]. Model studies showed that mode waters change their path and core PV in response to slow variations in wind, resulting in large subsurface temperature anomalies [*Xie et al.*, 2000; *Kubokawa and Xie*, 2002; *Hosoda et al.*, 2004]. The mechanism for STF variations is an interesting subject for future studies.

[52] The STF is commonly observed in other oceans. In the North Atlantic it is distributed near 25°–30°N in the western Sargasso Sea [e.g., *Reid*, 1978; *Olson et al.*, 1984; *Halliwel et al.*, 1994]. Subsurface front similar to those in the North Pacific STF is also found in the South Pacific, which is identified as a front accompanying the South Tropical Countercurrent [*Merle et al.*, 1969] in the latitudinal band 21°–29°S in the western subtropical gyre [*Qiu and Chen*, 2004]. These STFs seem to be associated with the STMW [*Hanawa and Talley*, 2001] on the poleward side, similar to the situation with the North Pacific northern STF. Comprehensive analyses on relationship between subsurface fronts and mode waters in these other oceans are to be made in the future.

[53] **Acknowledgments.** The main part of this work has been done when the first author was at the International Pacific Research Center (IPRC) at University of Hawaii and the Frontier Research System for Global Change (FRSGC). The authors would like to thank A. Kubokawa for many insightful discussions and N. Maximenko for providing the new data set of sea surface height used in Figure 4. The hydrographic data used in this study include the Far Seas Collection compiled by the National Research Institute of Far Seas Fisheries, Shimizu, Japan, and Russian data of the Far Eastern Regional Hydrometeorological Research Institute, provided courtesy by the Asia-Pacific Data Research Center (APDRC) of the IPRC. This work was partially supported by the Ministry of Education, Culture, Sports, Science and Technology, Japan [Grant-in-Aid for Young Scientists (B), 17740305] and Japan Agency for Marine-Earth Science and Technology. IPRC publication 406 and SOEST publication 6839.

References

- Aoki, Y., T. Suga, and K. Hanawa (2002), Subsurface subtropical fronts of the North Pacific as inherent boundaries in the ventilated thermocline, *J. Phys. Oceanogr.*, **32**, 2299–2311.
- Belkin, I. M., Z. Shan, and P. Cornillon (1998), Global survey of oceanic fronts from Pathfinder SST and in situ data, *Eos Trans. AGU*, **79**(45), Fall Meet. Suppl., Abstract OS31B-07.
- Conkright, M. E., et al. (2002a), World Ocean Data Base 2001, vol. 1, Introduction, edited by S. Levitus, *NOAA Atlas NESDIS 42*, 167 pp., U.S. Govt. Print. Off., Washington, D. C.
- Conkright, M. E., R. A. Locarnini, H. E. Garacia, T. D. O'Brien, T. P. Boyer, C. Stephens, and J. I. Antonov (2002b), World Ocean Atlas 2001: Objective analyses, data statistics, and figures, CD-ROM documentation, 17 pp., Natl. Oceanogr. Data Cent., Silver Spring, Md.
- Cushman-Roisin, B. (1981), Effects of horizontal advection on upper ocean mixing: A case of frontogenesis, *J. Phys. Oceanogr.*, **11**, 1345–1356.
- Cushman-Roisin, B. (1984), On the maintenance of the Subtropical Front and its associated countercurrent, *J. Phys. Oceanogr.*, **14**, 1179–1190.
- Dewar, W. K. (1992), Spontaneous shocks, *J. Phys. Oceanogr.*, **22**, 505–522.
- Halliwel, G. R., Jr., G. Peng, and D. B. Olson (1994), Stability of the Sargasso Sea subtropical frontal zone, *J. Phys. Oceanogr.*, **24**, 1166–1183.
- Hanawa, K., and L. D. Talley (2001), Mode waters, in *Ocean Circulation and Climate*, *Int. Geophys. Ser.*, edited by G. Siedler, J. Church, and J. Gould, pp. 373–386, Elsevier, New York.
- Hasunuma, K., and K. Yoshida (1978), Splitting the subtropical gyre in the western North Pacific, *J. Oceanogr. Soc. Jpn.*, **34**, 160–172.
- Hautala, S. L., and D. H. Roemmich (1998), Subtropical mode water in the Northeast Pacific Basin, *J. Geophys. Res.*, **103**(C6), 13,055–13,066.
- Hosoda, S., S.-P. Xie, K. Takeuchi, and M. Nonaka (2001), Eastern North Pacific subtropical mode water in a GCM: Formation mechanism and salinity effects, *J. Geophys. Res.*, **106**, 19,671–19,681.
- Hosoda, S., S.-P. Xie, K. Takeuchi, and M. Nonaka (2004), Interdecadal temperature variations in the North Pacific central mode water simulated by an OGCM, *J. Oceanogr.*, **60**, 865–877.
- Ichikawa, K., N. Gohda, M. Arai, and A. Kaneko (2004), Monitoring surface velocity from repeated ADCP observations and satellite altimetry, *J. Oceanogr.*, **60**, 365–374.
- Kobashi, F., and H. Kawamura (2001), Variation of sea surface height at periods of 65–220 days in the subtropical gyre of the North Pacific, *J. Geophys. Res.*, **106**, 26,817–26,831.
- Kobashi, F., and H. Kawamura (2002), Seasonal variation and instability nature of the North Pacific Subtropical Countercurrent and the Hawaiian Lee Countercurrent, *J. Geophys. Res.*, **107**(C11), 3185, doi:10.1029/2001JC001225.
- Kubokawa, A. (1995), Stationary Rossby waves and shocks on the Sverdrup coordinate, *J. Oceanogr.*, **51**, 207–224.
- Kubokawa, A. (1997), A two-level model of subtropical gyre and subtropical countercurrent, *J. Oceanogr.*, **53**, 231–244.
- Kubokawa, A. (1999), Ventilating thermocline strongly affected by a deep mixed layer: A theory for subtropical countercurrent, *J. Phys. Oceanogr.*, **29**, 1314–1333.
- Kubokawa, A., and T. Inui (1999), Subtropical countercurrent in an idealized ocean GCM, *J. Phys. Oceanogr.*, **29**, 1303–1313.
- Kubokawa, A., and S.-P. Xie (2002), On steady response of a ventilated thermocline to enhanced Ekman pumping, *J. Oceanogr.*, **58**, 565–575.
- Levitus, S., and T. P. Boyer (1994), World Ocean Atlas 1994, vol. 4, Temperature, *NOAA Atlas NESDIS 4*, 117 pp., U.S. Dep. of Commer., Washington, D. C.
- Levitus, S., R. Burgett, and T. P. Boyer (1994), World Ocean Atlas 1994, vol. 3, Salinity, 99 pp., *NOAA Atlas NESDIS 3*, U.S. Dep. of Commer., Washington, D. C.
- Masuzawa, J. (1969), Subtropical mode water, *Deep Sea Res.*, **16**, 436–472.

- Merle, J., H. Rotschi, and B. Voituriez (1969), Zonal circulation in the tropical western South Pacific at 170°E, *Bull. Jpn. Soc. Fish. Oceanogr., Professor Uda's Commem. Pap.*, 91–98.
- Nakamura, H. (1996), A pycnostad on the bottom of the ventilated portion in the central subtropical North Pacific: Its distribution and formation, *J. Oceanogr.*, 52, 171–188.
- Niiler, P. P., N. A. Maximenko, and J. C. McWilliams (2003), Dynamically balanced absolute sea level of the global ocean derived from near-surface velocity observations, *Geophys. Res. Lett.*, 30(22), 2164, doi:10.1029/2003GL018628.
- Oka, E., and T. Suga (2006), Differential formation and circulation of North Pacific central mode water, *J. Phys. Oceanogr.*, 35, 1997–2011.
- Olson, D. B., F. A. Schott, R. J. Zantopp, and K. D. Leaman (1984), The mean circulation east of the Bahamas as determined by a recent measurement program and historical XBT data, *J. Phys. Oceanogr.*, 14, 1470–1487.
- Qiu, B. (1999), Seasonal eddy field modulation of the North Pacific subtropical countercurrent: TOPEX/Poseidon observations and theory, *J. Phys. Oceanogr.*, 29, 2471–2486.
- Qiu, B., and S. Chen (2004), Seasonal modulations in the eddy field of the South Pacific Ocean, *J. Phys. Oceanogr.*, 34, 1515–1527.
- Qiu, B., and T. Durland (2002), Interaction between an island and the ventilated thermocline: Implications for the Hawaiian Lee Countercurrent, *J. Phys. Oceanogr.*, 32, 3408–3426.
- Qiu, B., D. A. Koh, C. Lumpkin, and P. Flament (1997), Existence and formation mechanism of the North Hawaiian Ridge current, *J. Phys. Oceanogr.*, 27, 431–444.
- Qu, T. (2002), Depth distribution of the subtropical gyre in the North Pacific, *J. Oceanogr.*, 58, 525–529.
- Reid, J. L. (1978), On the mid-depth circulation and salinity field in the North Atlantic Ocean, *J. Geophys. Res.*, 83, 5063–5067.
- Roden, G. I. (1975), On the North Pacific temperature, salinity, sound velocity fronts, and the relation to the wind and energy flux fields, *J. Phys. Oceanogr.*, 5, 557–571.
- Sakamoto, T., A. Sumi, S. Emori, T. Nishimura, H. Hasumi, T. Suzuki, and M. Kimoto (2004), Far-reaching effects of the Hawaiian Islands in the CCSR/NIES/FRCGC high-resolution climate model, *Geophys. Res. Lett.*, 31, L17212, doi:10.1029/2004GL020907.
- Stommel, H., and F. Schott (1977), The beta spiral and the determination of the absolute velocity field from hydrographic station data, *Deep Sea Res.*, 24, 325–329.
- Suga, T., and K. Hanawa (1995), The subtropical mode water circulation in the North Pacific, *J. Phys. Oceanogr.*, 25, 958–970.
- Suga, T., K. Hanawa, and Y. Toba (1989), Subtropical mode water in the 137°E section, *J. Phys. Oceanogr.*, 19, 1605–1618.
- Suga, T., Y. Takei, and K. Hanawa (1997), Thermocline distribution in the North Pacific subtropical gyre: The central mode water and the subtropical mode water, *J. Phys. Oceanogr.*, 27, 140–152.
- Suga, T., K. Motoki, Y. Aoki, and A. M. Macdonald (2004), The North Pacific climatology of winter mixed layer and mode waters, *J. Phys. Oceanogr.*, 34, 3–22.
- Takeuchi, K. (1984), Numerical study of the Subtropical Front and the Subtropical Countercurrent, *J. Oceanogr. Soc. Jpn.*, 40, 371–381.
- Talley, L. D. (1988), Potential vorticity distribution in the North Pacific, *J. Phys. Oceanogr.*, 18, 89–106.
- Uda, M., and K. Hasunuma (1969), The eastward subtropical countercurrent in the western North Pacific Ocean, *J. Oceanogr. Soc. Jpn.*, 25, 201–210.
- Welander, P. (1981), Mixed layer and fronts in simple ocean circulation model, *J. Phys. Oceanogr.*, 11, 148–152.
- White, W. B., and K. Hasunuma (1982), Quasi-stationary banded structure in the mean zonal geostrophic current regimes of the western North Pacific, *J. Mar. Res.*, 40, 1035–1046.
- White, W. B., and A. E. Walker (1985), The influence of the Hawaiian Archipelago upon the wind-driven subtropical gyre in the western North Pacific, *J. Geophys. Res.*, 90, 7061–7074.
- White, W. B., K. Hasunuma, and H. Solomon (1978), Large-scale seasonal and secular variability of the subtropical front in the western North Pacific from 1954 to 1974, *J. Geophys. Res.*, 83, 4531–4544.
- Xie, S.-P., T. Kunitani, A. Kubokawa, M. Nonaka, and S. Hosoda (2000), Interdecadal thermocline variability in the North Pacific for 1958–1997: A GCM simulation, *J. Phys. Oceanogr.*, 30, 2798–2813.
- Xie, S.-P., W. T. Liu, Q. Liu, and M. Nonaka (2001), Far-reaching effects of the Hawaiian Islands on the Pacific Ocean-atmosphere system, *Science*, 292, 2057–2060.
- Yoshida, K., and T. Kidokoro (1967a), A subtropical countercurrent in the North Pacific—An eastward flow near the Subtropical Convergence, *J. Oceanogr. Soc. Jpn.*, 23, 88–91.
- Yoshida, K., and T. Kidokoro (1967b), A subtropical countercurrent (II)—A prediction of eastward flows at lower subtropical latitudes, *J. Oceanogr. Soc. Jpn.*, 23, 231–236.
- Yu, Z., N. Maximenko, S.-P. Xie, and M. Nonaka (2003), On the termination of the Hawaiian Lee Countercurrent, *Geophys. Res. Lett.*, 30(5), 1215, doi:10.1029/2002GL016710.

F. Kobashi, Faculty of Marine Technology, Tokyo University of Marine Science and Technology, Etchujima 2-1-6, Koto-ku, Tokyo 135-8533, Japan. (kobashi@e.kaiyodai.ac.jp)

H. Mitsudera, Institute of Low Temperature Science, Hokkaido University, Sapporo 060-0819, Japan.

S.-P. Xie, International Pacific Research Center and Department of Meteorology, University of Hawaii, Honolulu, HI 96822, USA.